SIAM J. Applied Dynamical Systems
Vol. 4, No. 1, pp. 159–186


# Blinking Rolls: Chaotic Advection in a Three-Dimensional Flow with an Invariant*

P. Mullowney†, K. Julien†, and J. D. Meiss†

**Abstract.** We study a simple, nonautonomous, three-dimensional, incompressible flow corresponding to sequentially active two-dimensional rolls with distinct axes. A feature of the model is that an analytical map is obtained. We show that when the roll axes are orthogonal, motion is confined to two-dimensional topological spheres. The dynamics on each surface ranges from nearly regular to largely chaotic. We study the transport and mixing on each surface and their dependence upon parameters in the system.

**Key words.** chaotic advection, transport, mixing, volume-preserving mappings

**AMS subject classifications.** 76F25, 37B55, 70K55, 37D45

**DOI.** 10.1137/040606727

## 1. Introduction.

Fluid mixing corresponds to the transport of passive scalars by kinematic advection and their subsequent diffusive homogenization. Such phenomena are fundamentally important in many physical systems and engineering applications [36] and occur at a variety of scales ranging from the very small (micrometer scale) to the very large (planetary scales and beyond). For instance, mixing in microchannels can be used to efficiently homogenize reagents in chemical reactions even when the flow is laminar [41]. Understanding transport for planetary scale flows is critical for climate modeling and pollution dispersion in atmospheric science [8] and eddy dynamics in oceanography [23]. Transport and mixing are also important in granular flows [33], population biology [32, 39], and reaction-diffusion systems [35].

The mixing of tracer particles in a fluid flow is due to a combination of stirring and diffusion. In an efficient mixing process, stirring rapidly transports tracer elements by kinematic advection throughout the domain. The associated stretching and folding of material lines and surfaces ultimately trigger diffusive processes that homogenize the tracers into a blended mixture. Originally, it was assumed that mixing was most important in the context of turbulent flows where both processes are evident. However, as is now well known, effective mixing also occurs in laminar flows [2].

In three dimensions, these problems are especially challenging from a theoretical standpoint. One of the earliest advances came with the work on the Arnold–Beltrami–Childress (ABC) flow [13], an exact solution to the Euler equations. It was found that efficient stirring in three-dimensional incompressible flows can occur even for laminar and autonomous

*Received by the editors April 14, 2004; accepted for publication (in revised form) by M. Golubitsky July 18, 2004; published electronically February 22, 2005.
http://www.siam.org/journals/siads/4-1/60672.html
†Department of Applied Mathematics, University of Colorado, Boulder, CO 80309-0526 (paul.mullowney@colorado.edu, julien@colorado.edu, jdm@colorado.edu). The first author was supported by NSF VIGRE grant DMS-9810751. The second author was supported by an NSF grant OCE-0137347. The third author was supported in part by NSF grant DMS-0202032.

Eulerian velocity fields. Although the ABC flow is probably not physically observable, the crucial idea is that mixing can occur even in the simplest of flows in three dimensions [36]. In the two-dimensional case, transport can also be achieved in laminar, time-dependent flows. One of the seminal models was developed by Aref, who coined the term "chaotic advection" [1]. His flow, called the "blinking vortex," is specifically designed to yield nonintegrable Lagrangian trajectories. This model can be interpreted as an idealized mixing protocol where passive tracers are successively captured by the velocity fields of vortical stirrers that are the analogues of turbulent eddies with finite lifetimes.

In sections 2 and 3, we generalize the blinking vortex model and construct a physically motivated, yet mathematically simple, system with three-dimensional mixing. Our model, which we call "blinking rolls," replaces Aref's alternatively active vortices with alternatively active arrays of rolls aligned in different directions.

Though our mixing protocol is idealized, there is experimental evidence for the existence of similar flows. One such example is observed in Rayleigh–Bénard convection experiments for a binary mixture in a square cell with insulating sides. When the vertical temperature difference exceeds a threshold value, an instability leads to a sequence of temporally alternating, orthogonal convection rolls whose axes are parallel to the square boundaries [34]. It is observed that "the transition from one set of rolls to the other is very fast, followed by a relatively long period of domination by one of the rolls ... the system lies most of the time in the roll patterns." Another example of roll-switching is the Küppers–Lortz instability for rotating convection in a pure fluid [28, 9, 43, 22, 42]. Rotation causes an instability that results in switching of the roll axes by roughly 60°. Theoretical and experimental studies have shown that the rolls switch with a characteristic frequency proportional to the relative temperature difference above threshold.

When the switching occurs much faster than the roll turnover time, it can be idealized as instantaneous. In this case, the flow can be viewed as a composition of maps corresponding to the action of each individual roll. For the incompressible case, this gives a composition of volume-preserving maps. Transport in volume-preserving maps was studied in pioneering work on a discretized ABC system [37, 15, 12, 11]. The onset of transport is closely related to the destruction of heteroclinic connections for codimension-one manifolds [38, 29]; a Melnikov method was developed to study the bifurcations in manifold crossings in [30, 31].

It is generally difficult to find models for three-dimensional flows that both are mathematically accessible and have effective transport. However, there is a small but growing link between mixing in experimental, three-dimensional flows and theoretical modeling based on chaotic advection. Shinbrot and his collaborators have studied the transient behavior of weakly buoyant tracers in a laminar flow within a cylindrical batch stirring device using a traveling wave map with a buoyancy term [40]. In a similar though less symmetric device, a close link was found between the invariant regions of the flow visualized with a sheet laser and fluorescent dyes and the corresponding island chains of the Poincaré sections of a model [18, 19]. These examples reflect the growing evidence that mixing in three-dimensional flows can be effectively modeled via chaotic advection [36, 2]. This is crucial because it allows one to treat the flow as a low-dimensional dynamical system and thus bring to bear the geometrical and qualitative tools of dynamical systems theory.

In this paper, we present a theoretical and computational analysis for the blinking roll

model. In section 2 the flow for a single roll is constructed and the equations of motion are solved to obtain an analytical time-$t$ map. In section 3 the flow with roll-switching is modeled by composing several of these maps. For the case that the roll axes are orthogonal, there is an invariant that constrains the motion to two-dimensional surfaces. In fact, we show in section 4 that the invariant persists regardless of the choice of stirring protocol. This system has a number of symmetries that simplify its analysis; see section 5. In section 6, we use normal form expansions to understand behavior near a fixed point and near roll boundaries. Numerical results are given in section 7.

**2. Blinking rolls.** Aref's blinking vortex flow corresponds to a two-dimensional, inviscid, incompressible fluid in a circular domain of radius $a$ [1]. A point vortex moves inside the bounding contour according to a stirring protocol $(x(t), y(t))$. The equations for a passive scalar in such a fluid are Hamiltonian, and if the vortex position is constant in either a fixed or a steadily rotating coordinate system, then the flow is integrable. Otherwise, the flow is typically nonintegrable.

The blinking vortex corresponds to a stirring protocol with period $T$. For the first half of the period, a vortex resides at $(b, 0)$, and for the remainder of the period a vortex resides at $(-b, 0)$ for some $b < a$. For simplicity it is assumed that there is an instantaneous transition between the flows associated with the finite-lifetime point vortices. This allows the equations of motion for each half period to be solved exactly, giving rise to the half period maps $F_1(x, y)$ and $F_2(x, y)$. The Lagrangian tracer dynamics is then governed by the full period map $f = F_2 \circ F_1$.

Two-dimensional transport can then be studied simply by iterating the map. The dynamics are governed by two dimensionless parameters $\mu = \frac{\Gamma T}{2\pi a^2}$, representing the vortex strength, and $\beta = \frac{b}{a}$, its relative radial position. If $\beta$ is held fixed, then, for small enough $\mu$, chaotic advection is localized and there is no global transport. As $\mu$ increases, the chaotic regions grow and the phase portrait becomes increasingly homogenized.

Here we will construct a three-dimensional model analogous to the blinking vortex system. The model consists of flows generated by a succession of two-dimensional "rolls" aligned in distinct directions that are applied for alternating time intervals. By "roll," we mean the circulating flow associated with a vortical tube where the vorticity vector and the tube axis are aligned. We do not consider drift along the roll axes. The flow is thus invariant along the roll axis and can be represented in terms of a stream function $\psi$ with corresponding velocity field

$$\mathbf{v} = \nabla\psi(\mathbf{x}_\perp, t) \times \hat{\mathbf{e}}_\parallel, \tag{1}$$

where $\mathbf{e}_\parallel$ is the unit vector in the invariant direction. This generates motion in the $\mathbf{x}_\perp$-plane normal to $\mathbf{e}_\parallel$; if $\psi$ is autonomous, this motion is also confined to a two-dimensional surface defined by $\psi$ constant. Any critical point of the stream function, i.e., a point where $\nabla\psi = 0$, corresponds to a stationary axis. Near such an axis the flow is rotational whenever the critical point is an extrema; the circulation near such an axis corresponds to a *roll*.

We will primarily study the case of an array of trigonometric rolls; when they are aligned in the $x$ direction the stream function is given by

$$\psi = A\cos(y)\cos(z). \tag{2}$$

This gives the velocity field

$$(\dot{x}, \dot{y}, \dot{z}) = \nabla\psi(y, z) \times \hat{\mathbf{e}}_x = (0, -A\cos(y)\sin(z), A\sin(y)\cos(z)). \tag{3}$$

For this case, the line $(y, z) = (0, 0)$ is a roll axis (as are the axes $(m\pi, n\pi)$ for $m, n \in \mathbb{Z}$); nearby orbits lie on topological circles enclosing $x$-axis; see Figure 1. These circles limit on a square as $y$ and $z$ approach $\pm\frac{\pi}{2}$. The line $(y, z) = (\frac{\pi}{2}, \frac{\pi}{2})$ and its translations by $(m\pi, n\pi)$ correspond to saddle equilibria. Indeed the square cylinder boundary of the set $\{|y|, |z| \le \frac{\pi}{2}\}$ consists of the stable and unstable manifolds of the saddles, and it bounds the roll surrounding the $x$-axis by heteroclinic connections. If $A > 0$, the direction of rotation for this roll is right-handed or *positive*. If we translate by $\pi$ in a single direction, the direction of rotation becomes left-handed or *negative*.

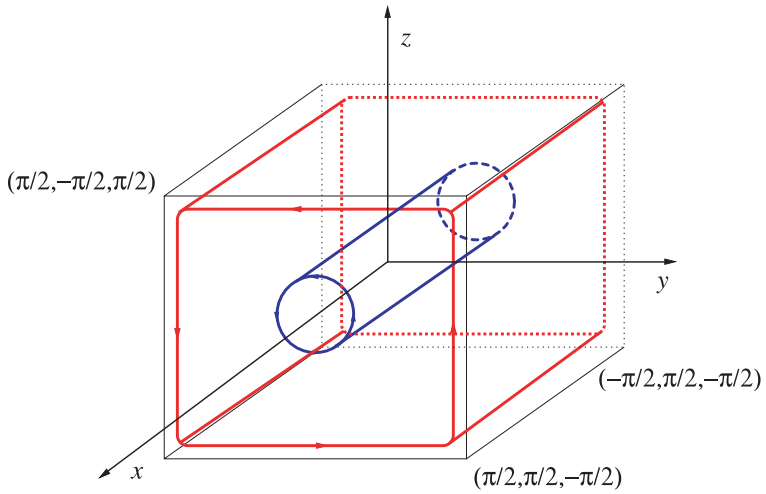


**Figure 1.** *Flow of a two-dimensional roll, $\psi_1(y, z)$, with positive rotation about the $x$-axis.*

A system of blinking rolls is obtained by alternatively switching between rolls aligned in different directions. A general mixing protocol can be implemented through a random specification of array lifetimes, amplitudes, and phases. However, for simplicity and as a preliminary investigation we restrict ourselves to roll arrays that are confined to a periodic lattice.

For example, consider three different roll arrays defined by stream functions $\psi_i, i = 1, 2, 3$, and axes $\hat{\mathbf{e}}_i$ aligned with the unit vectors of a Cartesian coordinate system. Each roll has a corresponding velocity field $v_i$ analogous to (3). Specifically, suppose that the roll $\psi_3$ is active for $0 \le t < T_3$, $\psi_2$ for $T_3 \le t < T_3 + T_2$, and $\psi_1$ for $T_3 + T_2 \le t < T_3 + T_2 + T_1$. We repeat this process periodically, so that the velocity field is time-periodic with period $T = T_1 + T_2 + T_3$. While any one roll array, say, $\psi_i$, is active, the motion is integrable, since $\psi_i$ is constant and is confined to a plane of constant $x_i$. However, as each roll array acts successively, one would expect that the trajectories should explore a fully three-dimensional domain.

More generally, we could allow the array of rolls to have arbitrary, multiplicative time

dependence, giving the general velocity field

$$\mathbf{v}(\mathbf{x},t) = A(t)\nabla\psi_1 \times \hat{\mathbf{e}}_1 + B(t)\nabla\psi_2 \times \hat{\mathbf{e}}_2 + C(t)\nabla\psi_3 \times \hat{\mathbf{e}}_3. \tag{4}$$

When $A(t)$, $B(t)$, and $C(t)$ are arbitrarily chosen, it is presumably impossible to solve explicitly for the flow. The blinking roll case corresponds to the choice of alternating step functions for $A(t)$, $B(t)$, and $C(t)$; see Figure 2. If we fix the functions $\psi_i$, then this system has six parameters, the times, $T_1$, $T_2$, and $T_3$, and the amplitudes of the step functions $A$, $B$, and $C$. The amplitudes of the roll arrays are analogous to the eddy strength $\Gamma$ in Aref's model.

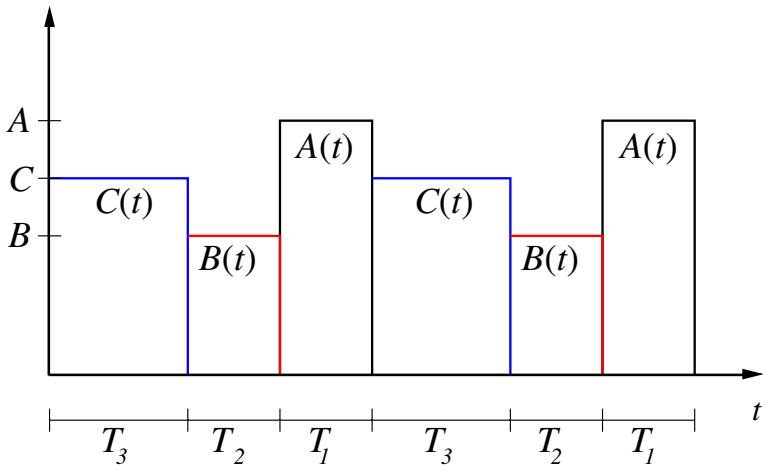


**Figure 2.** *Step functions $A(t)$, $B(t)$, and $C(t)$.*

Since only one roll array is active at any given time, if we can obtain an explicit solution for the flow of $\psi_i$, then we can construct an explicit time-$t$ map during the period that one array is active. We denote the time-$T_i$ map for the stream function $\psi_i$ by $F_i$:

$$F_i(x,y,z) = \Phi_{T_i}(x,y,z)\ , \quad \frac{d}{dt}\Phi_t = v_i(\Phi_t)\ , \quad \Phi_0 = id. \tag{5}$$

Here, the index $i$ of $F_i$ denotes the axis of rotation and the fixed direction under the map as well as the time of activation $T_i$. The blinking roll map is the composition of these maps:

$$(x',y',z') = F_1 \circ F_2 \circ F_3(x,y,z)\ . \tag{6}$$

Our next task is to obtain the explicit solutions for the flow in the case of (2).

**3. Blinking roll map.** In this section we construct the three-dimensional map for the velocity field (4) with rolls defined by (2) and amplitudes given by Figure 2. We begin by solving for the flow of a single roll to obtain an explicit time-$t$ map. Composition of the maps for each $\psi_i$ gives the full three-dimensional map (6).

The solution of the differential equations (3) can be easily obtained by noting that trajectories must satisfy $\frac{dy}{v_2} = \frac{dz}{v_3}$. The equations can be easily integrated in terms of Jacobi elliptic

functions [10] to obtain the flow

$$\Phi_t \begin{pmatrix} x \\ y \\ z \end{pmatrix} = \begin{pmatrix} x \\ \sin^{-1}(k\mathrm{sn}(At - M(y,z),k)) \\ \sin^{-1}(k\mathrm{sn}(At + N(y,z),k)) \end{pmatrix} , \tag{7}$$

where the elliptic function modulus is

$$k = \sqrt{1 - \cos^2(y)\cos^2(z)} \, . \tag{8}$$

The functions $M(y,z)$ and $N(y,z)$ are defined by setting $t = 0$ to get the initial condition, e.g., $\sin y = -k\mathrm{sn}(M,k)$ and $\sin(z) = k\mathrm{sn}(N,k)$. Though solving for $M$ and $N$ appears to require inversion of the elliptic functions, a much simplified expression that does not require this can be obtained by expanding sn using the sum formula [10]

$$\mathrm{sn}(\alpha+\beta) = \frac{\mathrm{sn}(\alpha)\mathrm{cn}(\beta)\mathrm{dn}(\beta) + \mathrm{sn}(\beta)\mathrm{cn}(\alpha)\mathrm{dn}(\alpha)}{1 - k^2\mathrm{sn}^2(\alpha)\mathrm{sn}^2(\beta)} \, .$$

Note that the time $t$ and amplitude $A$ occur only in the combination $At$ in (7). Thus if we rescale time by setting $T = At$, then we can eliminate the amplitude or roll strength parameter. As we would like to consider the possibility that $A < 0$, giving negative roll rotation, we allow $T$ to be negative. With this convention, the scaling is completely general. After scaling and simplification, the flow becomes

$$\Phi_T \begin{pmatrix} x \\ y \\ z \end{pmatrix} = \begin{pmatrix} x \\ \sin^{-1}\left(\frac{\sin(y)\mathrm{cn}(T)\mathrm{dn}(T) - \mathrm{sn}(T)\sin(z)\cos^2(y)}{1-\sin^2(y)\mathrm{sn}^2(T)}\right) \\ \sin^{-1}\left(\frac{\sin(z)\mathrm{cn}(T)\mathrm{dn}(T) + \mathrm{sn}(T)\sin(y)\cos^2(z)}{1-\sin^2(z)\mathrm{sn}^2(T)}\right) \end{pmatrix} . \tag{9}$$

Equation (9) depends explicitly on the initial condition, and the modulus is still given by (8). Since typical numerical algorithms for Jacobi elliptic functions give sn, dn, and cn simultaneously [16], having all three in the expression (9) has no additional numerical cost.

Since the amplitude has been scaled out, $\mathrm{sgn}(T)$ controls the direction of rotation of $\Phi_T$, which of course satisfies the flow property $\Phi_{-T} = \Phi_T^{-1}$. Since cn and dn are even and sn is odd, the only term that is affected by the switch in rotation direction is the second term in the numerator of each fraction in (9). By setting $T = T_1$, we get the time-$T_1$ map (5)

$$F_1(x,y,z) = \Phi_{T_1}(x,y,z)$$

from (9).

To obtain a three-dimensional map for blinking rolls, we consider the velocity field (4) with $A(t)$, $B(t)$, and $C(t)$ alternating, periodic step functions defined as in Figure 2 and all three of the stream functions of analogous form to (2). All of the amplitudes can be removed by rescaling time; therefore, without loss of generality, we can set $A = B = C = 1$, leaving only the three parameters $T_1$, $T_2$, and $T_3$. Of course, the signs of these parameters represent the direction of rotation of the rolls. The maps $F_2$ and $F_3$ in (6) are obtained easily from (9) by permuting the variables appropriately.

**4. Existence of an invariant.** Our numerical investigations for blinking orthogonal roll arrays indicate that three-dimensional mixing does not occur (see section 7). Indeed, these investigations led to the discovery that the flow has an invariant for this case. This was unexpected since invariants are not common for volume-preserving flows and mappings that have no apparent symmetries (though some special examples have been constructed in [20]). As we see here, the flow of (4) does have a symmetry, although it is not immediately obvious.

Indeed, there is an invariant for the case of three rolls if we choose the stream functions to have the separable forms

$$\psi_1 = g(y)h(z), \quad \psi_2 = f(x)h(z), \quad \psi_3 = f(x)g(y). \tag{10}$$

In this case it is easy to see that for *arbitrary* amplitude functions $A(t), B(t)$, and $C(t)$ (i.e., *arbitrary* stirring protocol), the function

$$J = f(x)g(y)h(z) \tag{11}$$

is an invariant for the flow. To see this in a pedestrian way, one need only show that

$$\frac{dJ}{dt} = \nabla J(\mathbf{x}) \cdot \mathbf{v}(\mathbf{x}, t) = 0, \tag{12}$$

as is easy to demonstrate using (4).

More generally, if $\nabla J \neq 0$, then (12) implies that there exists a vector field $\mathbf{E}(\mathbf{x}, t)$ such that [7]

$$\mathbf{v}(\mathbf{x}, t) = \nabla J \times \mathbf{E}(\mathbf{x}, t). \tag{13}$$

This flow is volume-preserving providing

$$\nabla \cdot \mathbf{v} = -\nabla J \cdot (\nabla \times \mathbf{E}(\mathbf{x}, t)) = 0.$$

One solution of this is $\mathbf{E} = \nabla\varphi(\mathbf{x}, t)$.[1] If $\varphi$ were time-independent, then it would also be an invariant, and the flow would be integrable. However, if the velocity depends upon time, there need not be a second invariant (as we will see in section 7). For example, the field $\mathbf{E} = (E_x(x, t), E_y(y, t), E_z(z, t))$ is curl-free, and the resulting velocity field is a superposition of the roll-like terms $v_i = E_{x_i}(x_i, t)\nabla J \times \hat{\mathbf{e}}_i$. The velocity of (4) with the separable stream functions (10) is obtained by choosing a suitable $J$ of the form (11) and

$$\mathbf{E} = \left(\frac{A(t)}{f(x)}, \frac{B(t)}{g(y)}, \frac{C(t)}{h(z)}\right).$$

When written in this way, the invariance of $J$ is rather obvious from (13).

For cosine rolls, we choose $f = g = h = \cos$, and the invariant is

$$J = \cos(x)\cos(y)\cos(z). \tag{14}$$

The invariant surfaces, shown in Figure 3, are nested topological spheres centered at the origin that become cube-like near the boundary given by $x = \pm\frac{\pi}{2}$, $y = \pm\frac{\pi}{2}$, or $z = \pm\frac{\pi}{2}$. Since there is an invariant, the trajectories are confined to these surfaces, and there will be no three-dimensional mixing. However, the flow still exhibits considerable complexity as we will see in section 7.

[1] More generally, $\mathbf{E}$ need not be curl-free—its curl must only be tangent to the surfaces of constant $J$.

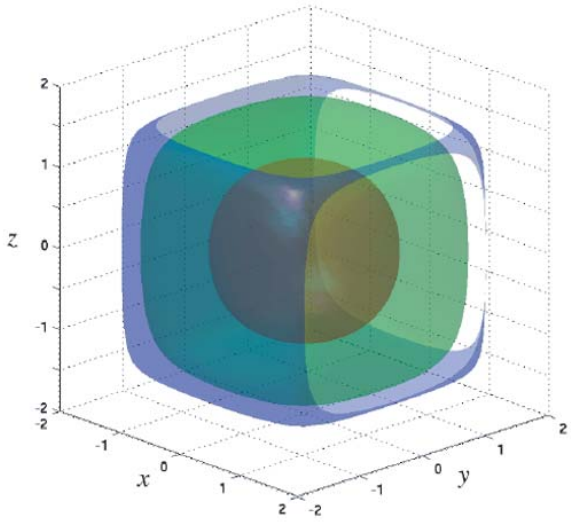


**Figure 3.** *Three level sets of the invariant* (14)*. The gaps in the outer surface are used to illustrate the concentric structure of the level sets.*

**5. Symmetries.** The trigonometric roll (3) is periodic with period $2\pi$ and is odd under translation by $\pi$ in $y$ or $z$. This implies that the fundamental cube for the three-dimensional flow (4) is divided into eight cells with alternating rotation directions; the case that all $T_i > 0$ is shown in Figure 4. The $\pm$ signs in the figure indicate the directions of right- (left-) handed rotation for each roll, respectively.

The flows in the eight cells are equivalent, as we can see by considering symmetries of the vector field. A map $R$ is a symmetry of a vector field $\mathbf{v}$ if $DR^{-1} \circ \mathbf{v} \circ R = \mathbf{v}$. It is easy to see that the velocity for trigonometric rolls has the four symmetries

$$\begin{aligned} R(x,y,z) &= (-x,-y,-z), & P_1(x,y,z) &= (x+\pi,-y,-z), \\ P_2(x,y,z) &= (-x,y+\pi,-z), & P_3(x,y,z) &= (-x,-y,z+\pi), \end{aligned} \tag{15}$$

corresponding to a reflection through the origin ($R$), and translations of $x_i$ by $\pi$ with a reflection through a perpendicular plane ($P_i$). There are also symmetries from $2\pi$ translations. The group of symmetries generated by (15) is Abelian and has sixteen elements. Taking into account the $2\pi$ periodicity, this group of symmetries maps the flow in the cell $|x|, |y|, |z| < \frac{\pi}{2}$ onto the other seven cells.

Note that there are two possible structures—one corresponding to the choice of all positive times $T_i$ as shown in Figure 4, and the other to all negative times, created by flipping the signs of each roll. There does not seem to be any way to map $(+++)$ onto $(---)$. To see this, let $t \to -t$. Then, in order for the velocity field (4) to remain unchanged under time reversal transformations, the functions $A(t)$, $B(t)$, and $C(t)$ must be odd. This contradicts the definitions given in section 2. Thus there are two signed cases that should be considered to obtain all possible behaviors.

A numerical study of the behavior depending upon all three parameters is tedious. In

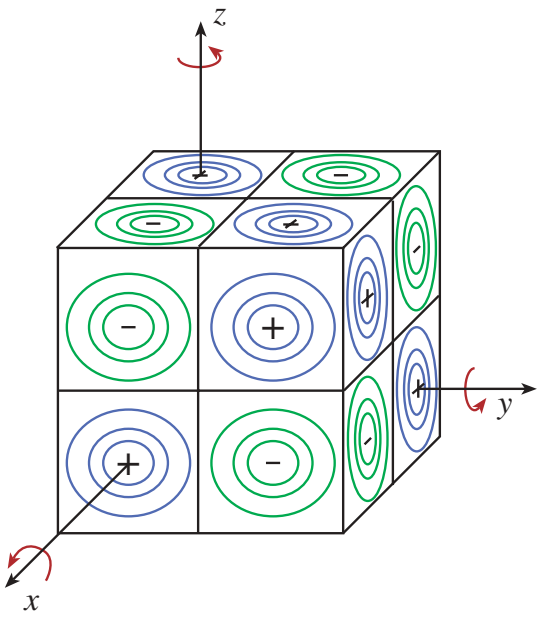


**Figure 4.** *Fundamental cube ( $-\frac{\pi}{2} < x, y, z < \frac{3\pi}{2}$ ) showing the topology of the cosine rolls on the respective faces when $T_i > 0$. The + sign stands for a right-handed rotation and the − for a left-handed rotation. Note that for a general mixing protocol, the roll arrays can be simultaneously active, although a time-t map cannot be constructed in this case.*

section 7 we will primarily study a two-roll map

$$F_{ij} = F_i \circ F_j \tag{16}$$

for some choice of $i$ and $j$. We will now show that, without loss of generality, we can restrict consideration to a single choice of the indices $i, j$, say, $i = 1$ and $j = 3$, and to the case that $T_1 > T_3 > 0$. We do this by exploiting some of the obvious symmetries of (16).

It is trivial to show conjugacies between (16) and three other maps: $F_i^{-1} \circ F_j^{-1}$, $F_i \circ F_j^{-1}$, and $F_i^{-1} \circ F_j$. This is accomplished by defining $S_i$ and $H_i$ (for $i = 1, 2, 3$) as

$$S_1(x, y, z) = (x, -z, y), \qquad H_1(x, y, z) = (-x, y, z),$$

plus cyclic permutations. Here the map $S_i$ is a positive rotation by $\frac{\pi}{2}$ about the $i$th axis, and $H_i$ is a reflection about the plane perpendicular to the $i$th axis. Thus $H_i^2 = id$ and $H_i \circ H_j = H_j \circ H_i$. A simple calculation then shows that

$$S_i \circ F_i \circ S_i^{-1} = F_i, \qquad H_i \circ F_i \circ H_i = F_i.$$

Applying the $i$th rotation to the $j$th map gives

$$S_1^{-1} \circ F_2 \circ S_1 = S_2 \circ F_1 \circ S_2^{-1} = F_3^{-1},$$
$$S_1 \circ F_2 \circ S_1^{-1} = S_2^{-1} \circ F_1 \circ S_2 = F_3,$$

and all cyclic permutations. Similarly, for the reflection,

$$H_1 \circ F_2 \circ H_1 = F_2^{-1}, \qquad H_1 \circ F_3 \circ H_1 = F_3^{-1},$$

and all cyclic permutations. Using these, we obtain

$$H_k \circ F_i \circ F_j \circ H_k = \begin{cases} F_i^{-1} \circ F_j & \text{if } k = j \neq i, \\ F_i \circ F_j^{-1} & \text{if } k = i \neq j, \\ F_i^{-1} \circ F_j^{-1} & \text{if } k \neq i \text{ and } k \neq j. \end{cases} \tag{17}$$

From this we conclude that once a particular $i$ and $j$ are picked, the direction of rotation for each component is irrelevant because the maps are all conjugate to one another.

We next show that maps with different choices of $i$ and $j$ are conjugate. As the axes can be mapped onto each other by rotations, we consider

$$S_k^{-1} \circ F_i(T_i) \circ F_j(T_j) \circ S_k \quad \text{for } \ i \neq j,$$

which switches one or both axes of rotation depending upon the choice of $k$. Here we have explicitly put in the parameter $T$, since it will be important below. First, for the case $k = i$,

$$S_i^{-1} \circ F_i(T_i) \circ F_j(T_j) \circ S_i = \begin{cases} F_i(T_i) \circ F_{i-2}(T_j) & \text{if} \quad j = i - 1, \\ F_i(T_i) \circ F_{i+2}^{-1}(T_j) & \text{if} \quad j = i + 1, \end{cases}$$

where the indices are understood modulus 3. Next, if $k = j$, then

$$S_j^{-1} \circ F_i(T_i) \circ F_j(T_j) \circ S_j = \begin{cases} F_{j-2}(T_i) \circ F_j(T_j) & \text{if} \quad i = j - 1, \\ F_{j+2}^{-1}(T_i) \circ F_j(T_j) & \text{if} \quad i = j + 1. \end{cases}$$

Combining these relations with (17) shows that maps with all possible choices of different axes and different rotation directions are conjugate to one another. The critical point is that the first roll must be active for time $T_j$, and the second roll must be active for $T_i$ as stated originally in (16).

Finally, for the case when $k \neq j \neq i$, we find

$$\begin{aligned} S_k^{-1} \circ F_i(T_i) \circ F_j(T_j) \circ S_k &= \begin{cases} F_j^{-1}(T_i) \circ F_i(T_j) & \text{if} \quad k = j + 1, \\ F_j(T_i) \circ F_i^{-1}(T_j) & \text{if} \quad k = j - 1 \end{cases} \\ &\cong F_j^{-1}(T_i) \circ F_i^{-1}(T_j) \quad \text{by (17)} \\ &= (F_i(T_j) \circ F_j(T_i))^{-1}. \end{aligned}$$

Thus $F_{ij}$ is conjugate to its inverse with time parameters swapped. Since orbits are mapped to orbits under inversion (and the maps are bijections), the phase portrait of the dynamics of the map $F_i(T_i) \circ F_j(T_j)$ will appear conjugate to that of $F_i(T_j) \circ F_i(T_i)$.

In conclusion, for the two-roll map (16) the direction of rotation is irrelevant so that only positive times need to be considered. Moreover, the choice of particular axes of rotation is irrelevant (so long as they are different). Finally, only the case $T_i > T_j$ need be studied, because the original map is conjugate to its inverse with time parameters swapped.

**6. Normal forms.** The dynamics of (6) near the origin and on the boundary of the fundamental cube is relatively simple. In this section we use a normal form expansion near the origin to explore the effect of the nonlinear terms on the elliptic fixed point. We will show that when the map has an invariant, the dynamics near the origin are especially simple: the orbits of the normal form lie on invariant circles. To study the motion on the boundary of the fundamental cube, we use the fact that (9) reduces to a pair of one-dimensional maps analogous to shear flow on appropriate pieces of the boundary ($y = \pm\frac{\pi}{2}$ and/or $z = \pm\frac{\pi}{2}$). This implies that for (6), the dynamics on the boundary are relatively simple.

**6.1. Motion near the origin.** The asymptotic behavior of a map near a fixed point can be profitably studied using normal forms [3]. Normal forms were introduced by Birkhoff for the area-preserving case [6]; similar forms for volume-preserving mappings near a fixed point have been studied by Bazzani [4] and Bazzani and Di Sebastiano [5]. The analysis in these papers excludes the case that the fixed point is linearly stable, which is of interest to us, so we explain some of the details of the calculation here.

The linear behavior of (6) near the origin is governed by the Jacobian matrix

$$DF(0) = DF_1(0)\, DF_2(0)\, DF_3(0).$$

It is straightforward to see that the Jacobian of (9) at the origin is

$$D\Phi_T(0) = \begin{pmatrix} 1 & 0 & 0 \\ 0 & \cos(T) & -\sin(T) \\ 0 & \sin(T) & \cos(T) \end{pmatrix}.$$

This implies that each $DF_i$ is a rotation about the axis $\hat{e_i}$ by angle $T_i$ and therefore that $DF(0) \in SO(3)$. It is well known that any special orthogonal matrix is a rotation about some axis; therefore, $DF(0)$ must have a complex conjugate pair of eigenvalues with modulus one

$$\lambda_{1,2} = e^{\pm 2\pi i\omega},$$

and one unit eigenvalue $\lambda_3 = 1$, with eigenvector $v_3$ corresponding to the rotation axis. In our case, we find that

$$\cos(2\pi\omega) = \frac{1}{2}(\sin T_1 \sin T_2 \sin T_3 + \cos T_1 \cos T_2 + \cos T_2 \cos T_3 + \cos T_3 \cos T_1 - 1).$$

Thus $DF(0)$ is a rotation about the axis $v_3$ with angle $2\pi\omega$.

The first step in a normal form transformation is to diagonalize the linear system. We can diagonalize $DF(0)$ using a complex coordinate transformation $(x, y, z) \to (u, \bar{u}, w)$, where $w$ represents the coordinate along the eigenvector $v_3$, $u$ is the complex coordinate in the perpendicular plane, and $\bar{u}$ is the complex conjugate. The linearization then becomes

$$(u', \bar{u}', w') = \Lambda(u, \bar{u}, w), \quad \Lambda = \begin{pmatrix} e^{2\pi i\omega} & 0 & 0 \\ 0 & e^{-2\pi i\omega} & 0 \\ 0 & 0 & 1 \end{pmatrix}.$$

We denote the map in the new coordinates $\mathbf{u} = (u, \bar{u}, w)$ by $\mathcal{F}$, so that $D\mathcal{F}(0) = \Lambda$. Expand $\mathcal{F}$ in a power series expansion of the form

$$\mathcal{F}(\mathbf{u}) = \Lambda(\mathbf{u} + \mathcal{F}^{(k)}(\mathbf{u}) + \mathcal{F}^{(k+1)}(\mathbf{u}) + \cdots),$$

where $\mathcal{F}^{(k)}$ is a term that is homogeneous of degree $k > 1$ in the variables $\mathbf{u}$, i.e.,

$$\mathcal{F}^{(k)} = \sum_{m+n+p=k} a_{m,n,p} u^m \bar{u}^n w^p , \tag{18}$$

with $m, n, p \in \mathbb{Z}_+$, and complex coefficients $a_{m,n,p}$. Since the original map is real, $\bar{u}$ is the complex conjugate of $u$, and thus $\bar{a}_{m,n,p} = a_{n,m.p}$.

The normal form for $\mathcal{F}$ is a "simpler" map $\mathcal{G}$ that is conjugate to $\mathcal{F}$,

$$\mathcal{G}(h(\mathbf{u})) = h(\mathcal{F}(\mathbf{u})), \tag{19}$$

by a near identity transformation $h$. As usual we expand the conjugacy $h$ and the new map in power series and at each order use $h$ to remove as many terms in $\mathcal{G}$ as possible. At order $k$ all terms in $\mathcal{F}^{(k)}$ can be removed except those that are "resonant," i.e., those terms in the $q$th component of (18) for which the integers satisfy

$$\lambda_1^m \lambda_2^n \lambda_3^p = e^{2\pi i(m-n)\omega} = \lambda_q. \tag{20}$$

For each $\omega$, we denote the solutions of (20) by $R$, and the normal form becomes

$$\mathcal{G} = \Lambda(\mathbf{u} + \mathcal{F}_R^{(k)}(\mathbf{u}) + \cdots),$$

where $\mathcal{F}_R^{(k)}$ denotes those terms in (18) for which $m, n, p$ are in $R$.

When $\omega$ is irrational, (20) shows that resonances occur when

$$\begin{aligned} m &= n + 1 \quad \text{for } q = 1, \\ m &= n - 1 \quad \text{for } q = 2, \\ m &= n \quad\;\; \text{for } q = 3. \end{aligned}$$

Since we can eliminate the nonresonant terms to all orders, the normal form becomes

$$\begin{aligned} u' &= e^{2\pi i\omega} u \left( 1 + \sum_{n,p\geq 0} \alpha_{2n,p} |u|^{2n} w^p \right), \\ w' &= w \left( 1 + \sum_{n,p\geq 0} \beta_{2n,p-1} |u|^{2n} w^{p-1} \right), \end{aligned} \tag{21}$$

where $\beta_{n,p}$ is real and $\alpha_{0,0} = \beta_{0,0} = 0$, since the corrections must be nonlinear. As is true for general normal form theory, (21) commutes with the group generated by $\Lambda$ [14]; since we assumed $\omega$ is irrational, it commutes with arbitrary rotations about the $w$-axis. Note that the series (21) is not guaranteed to converge, even in some neighborhood of the origin, and thus must be viewed only in an asymptotic sense.

As demonstrated in section 5, the map (6) has reflection symmetry through the origin. In this case, the normal form will exhibit the same symmetry, and therefore all even order terms drop out of the expansion so that

$$\alpha_{2n,2p+1} = \beta_{2n,2p+1} = 0.$$

In addition, if $F$ is volume-preserving, then we can choose $h$ so that it also preserves volume, and therefore the normal form will as well:

$$du' \wedge d\bar{u}' \wedge dw' = du \wedge d\bar{u} \wedge dw.$$

This places restrictions on the coefficients of (21). To cubic order, we find

$$\beta_{2,0} = -4\mathrm{Re}(\alpha_{2,0}), \qquad \beta_{0,2} = -\frac{2}{3}\mathrm{Re}(\alpha_{0,2}). \tag{22}$$

Now, we can analyze basic phenomena of the normal form. Letting $u = \rho e^{2\pi i\theta}$, we can rewrite (21) to obtain the real map

$$\begin{aligned}
\rho' &= \rho\left(1 - \frac{1}{4}\beta_{2,0}\rho^2 - \frac{3}{2}\beta_{0,2}w^2 + O(3)\right),\\
\theta' &= \theta + \omega + \mathrm{Im}(\alpha_{2,0})\rho^2 + \mathrm{Im}(\alpha_{0,2})w^2 + O(3),\\
w' &= w(1 + \beta_{2,0}\rho^2 + \beta_{0,2}w^2 + O(3)).
\end{aligned}$$

Thus the origin is a nonhyperbolic fixed point. To all orders, the $w$-axis ($\rho = 0$) and the equatorial plane $w = 0$ are invariant. The plane $w = 0$ is locally an (un)stable manifold of the origin when $\beta_{2,0} > 0$ ($< 0$), and the $w$-axis is locally (un)stable when $\beta_{0,2} < 0$ ($> 0$). There are additional unstable manifolds along the lines $\rho = sw$ when $s^2 = -2\frac{\beta_{0,2}}{\beta_{2,0}} > 0$, and these are (un)stable manifolds when $\beta_{0,2} > 0 (< 0)$. An example is shown in Figure 5.

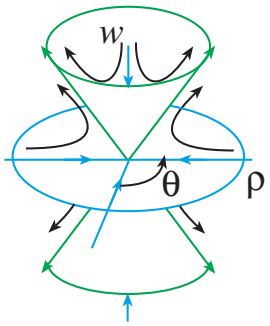


**Figure 5.** *Dynamics of the normal form in the $(\rho, w)$-plane for $\beta_{2,0} > 0$ and $\beta_{0,2} < 0$.*

Note that when there is an invariant whose surfaces are topological spheres about the origin (as is the case for (6)), none of the invariant axes can be attracting or repelling. Thus the only normal form that corresponds to this case is one in which *every* resonant coefficient has real part zero. Thus the normal form for (6) with irrational $\omega$ fixes $\rho$ and $w$, and every orbit near the origin lies on an invariant circle. As we will see, this corresponds well with the numerical observations of the dynamics of (6) in section 7.

**6.2. Motion on the boundary cube.** The single roll flow (9) preserves the boundaries of the fundamental cube; the surfaces where $x$, $y$, or $z$ are $\pm\frac{\pi}{2}$. Recall from section 2 that the line $(y,z)=(\frac{\pi}{2},\frac{\pi}{2})$ and its translations by $(m\pi,n\pi)$ consist of saddle equilibria of $\Phi_T$. The four faces corresponding to the set $\{(y,z):|y|=\frac{\pi}{2}\ or\ |z|=\frac{\pi}{2}\}$ correspond to their stable and unstable manifolds.

On these faces, the velocity field (3) has only one component, and its flow simplifies since there the modulus $k\to 1$, and $\mathrm{sn}(T,1)=\tanh(T)$, and $\mathrm{cn}(T,1)=\mathrm{dn}(T,1)=\mathrm{sech}(T)$. In this case (9) becomes

$$\Phi_T(x,y,z)=\begin{cases}\left(x,y,\sin^{-1}\left(\frac{\cosh(T)\sin(z)\pm\sinh(T)}{\cosh(T)\pm\sin(z)\sinh(T)}\right)\right) & \text{if } y=\pm\frac{\pi}{2},\\ \left(x,\sin^{-1}\left(\frac{\cosh(T)\sin(y)\mp\sinh(T)}{\cosh(T)\mp\sin(y)\sinh(T)}\right),z\right) & \text{if } z=\pm\frac{\pi}{2}.\end{cases}\tag{23}$$

This formula for $T=T_1$ gives the boundary map corresponding to $F_1$; we denote it as $B_1$. The maps $B_2$ and $B_3$ are obtained from (23) by permuting the variables appropriately.

It is convenient to use a spherical projection to display the dynamics of the system. Letting $(\theta,\eta)$ denote the longitude and colatitude, respectively, we can project the cube onto the sphere. Then the dynamics can be displayed on the rectangle $-\pi<\theta\le\pi$, $0\le\eta\le\pi$. For example, in Figure 6 we show $F_1$ and $F_3$ in this projection. In this figure, the twelve edges of the cube project to the red curves. The faces $x=\pm\frac{\pi}{2}$ are pierced in the center by the points $(\theta,\eta)=(0,\frac{\pi}{2})$ and $(\theta,\eta)=(\pi,\frac{\pi}{2})$, respectively. The faces defined by $z=\pm\frac{\pi}{2}$ correspond to those with $\eta$ near 0 and $\pi$. The remaining panels define $y=\pm\frac{\pi}{2}$.

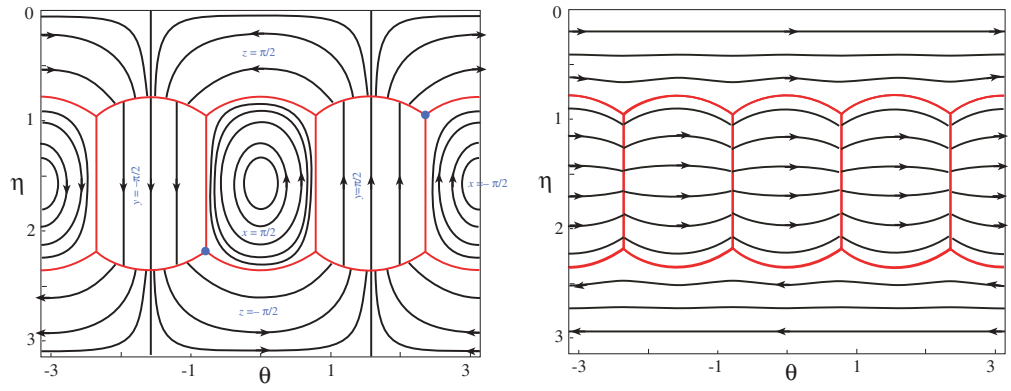


**Figure 6.** *Maps on the boundary cube projected onto the spherical angles $(\theta,\eta)$. Invariant curves of $F_1$ are shown in the left panel and those of $F_3$ are shown in the right. Note that the two figures are equivalent under a positive rotation by $\frac{\pi}{2}$ about the y-axis.*

Now consider the two-roll composition

$$F_1\circ F_3.$$

Since the cube is an invariant surface for each map, it is still invariant. The eight vertices, $v_{\pm\pm\pm}=(\pm\pi/2,\pm\pi/2,\pm\pi/2)$, are saddle fixed-points. These points are represented by the

intersections of the red curves in Figure 6. The edges of the cube now comprise parts of the stable or unstable manifolds of the saddle fixed-points.

On the two faces defined by $y = \pm\frac{\pi}{2}$, the boundary behavior is given by $B_1 \circ B_3$ because both of the moduli of the corresponding flows are one. Figure 6 shows simple dynamics on this face corresponding to shear flows. The face $y = \frac{\pi}{2}$ is a branch of the stable manifold of the saddle $v_{-++}$ (shown as a blue dot in Figure 6). Similarly, the boundary face $y = -\frac{\pi}{2}$ is a branch of the stable manifold of $v_{+--}$. The Jacobian at the vertices is easily evaluated by linearizing the flow at a saddle equilibrium to obtain $DF_1 = \mathrm{diag}(1, e^{s_1 T_1}, e^{-s_1 T_1})$, where $s_1 = \mathrm{sgn}(yz)$, and $DF_3 = \mathrm{diag}(e^{s_3 T_3}, e^{-s_3 T_3}, 1)$, where $s_3 = \mathrm{sgn}(xy)$. Thus at the vertex $v_{-++}$

$$DF_1 \circ DF_3 = \mathrm{diag}(e^{-T_3}, e^{T_1+T_3}, e^{-T_1}). \tag{24}$$

On the four remaining faces, the dynamics is determined by either $F_1 \circ B_3$ or $B_1 \circ F_3$, and even these simplified maps can have complicated behavior. Here we will discuss the existence of fixed points. For example consider $F_1 \circ B_3$ on the face $x = \pi/2$. In the simplest case, when $T_3 = 0$, the dynamics is simply the sheared rotation defined by the single roll. The rotation number of $F_1$ is

$$\omega = \frac{T_1}{4K(k)},$$

where $K$ is the complete elliptic integral, and $k$ is the modulus (8). Since $K(0) = \frac{\pi}{2}$, $\omega$ starts at $\frac{T_1}{2\pi}$ at $(\frac{\pi}{2}, 0, 0)$ and decreases to zero at the edges; therefore, there will be fixed points at the center of the face and on any streamline for which $\omega$ is an integer. If we restrict our attention to $0 < T_1 < 2\pi$, there is exactly one elliptic fixed point on the face—the point $(\frac{\pi}{2}, 0, 0)$. Moreover, the implicit function theorem implies that this fixed point persists for $T_3$ nonzero, since the elliptic fixed points have eigenvalues not equal to 1.

Because $B_3$ is applied before $F_1$ and we are considering only rolls with positive rotation, all fixed points reside on the $y < 0$ half of the face $x = \frac{\pi}{2}$. Since the streamlines of $F_1$ are symmetric about the plane $y = 0$, and $B_3$ changes $y$ only, any fixed point must occur on a line $y = -c$ such that $B_3(-c, z) = (c, z)$, and correspondingly, we must have $F_1(c, z) = (-c, z)$. The points $(\pm c, z)$ reside on the same streamline of $F_1$, and therefore there must be a $T_1$ such that $F_1(c, z) = (-c, z)$ (up to $4K$ periodicity) because the curves are continuous, closed loops.

Indeed, for large enough values of $T_1$ there can be multiple fixed points on this face. To see this, consider the vertical line segments $l_\pm = \{(y = \pm c, z)\}$; see Figure 7. For each $c$, there exists a $T_3$ such that $B_3(l_-) = l_+$. The image of $l_+$ under $F_1$ can be quite complex. As shown in the figure, if $T_1 < T_3$, $F_1(l_+)$ does not intersect $l_-$, and there are no fixed points on the face. For $T_1 = T_3$ , $F_1(l_+)$ (the red curve) intersects $l_-$ at $z = \frac{\pi}{2}$. When $T_1$ is slightly greater than $T_3$, we have at most one fixed point because there is only one intersection; however, if $T_1 >> T_3$ (the cyan curve), there can be many fixed points. If there is one intersection, then this point is actually a fixed point, as symmetry implies that $F_1(c, z) = (-c, z)$. However, if $F_1(l_+)$ intersects $l_-$ in several places, not all intersections need have the same $z$ coordinate after iteration. When there exist more than three such intersections, then some of them can be candidates for additional fixed points.

One can understand fixed points on the other faces by a similar argument.

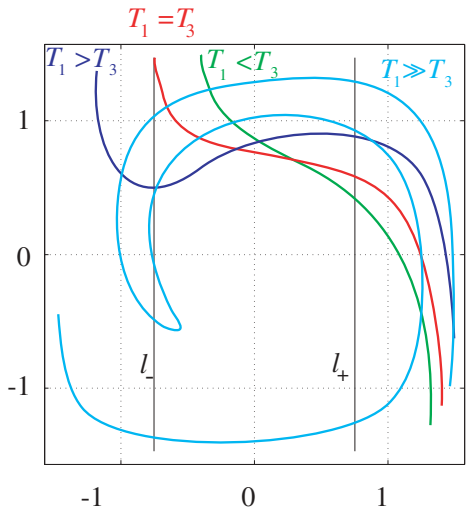


**Figure 7.** *Fixed points of $F_1 \circ B_3$ at $x = \frac{\pi}{2}$. Here $l_+ = B_3(l_-)$ and the colored curves are images of $l_+$ under $F_1$.*

**7. Numerical explorations.** In this section we will explore some of the dynamics (6). For simplicity, we set $T_2 = 0$ so that the second roll is not active, giving the system

$$F = F_1 \circ F_3. \tag{25}$$

As we showed in section 5, it is sufficient to consider to $T_1 > T_3 > 0$.

First we discuss the techniques that we will use to visualize the orbits of (25). We take advantage of the fact that orbits are constrained to surfaces of constant $J(x, y, z) = \cos(x)\cos(y)\cos(z)$, and that for each $0 < J \leq 1$ these surfaces are convex, topological spheres; recall Figure 3. Therefore, as we did in section 6.2 for the maps on the boundary, we can use spherical coordinates to obtain a two-dimensional projection of the dynamics. Letting $(\theta, \eta)$ be the spherical angles, any point $(x, y, z)$ corresponds to a point $(J, \theta, \eta)$, and since $J$ is invariant, we can view the dynamics in the angle plane. The coordinate transformation is thus

$$(J, \theta, \eta) = V(x, y, z) = \left(\cos(x)\cos(y)\cos(z), \tan^{-1}\left(\frac{y}{x}\right), \tan^{-1}\left(\frac{\sqrt{x^2+y^2}}{z}\right)\right), \tag{26}$$

which has the Jacobian

$$\det(DV) = J\frac{x\tan x + y\tan y + z\tan z}{\sqrt{x^2+y^2}(x^2+y^2+z^2)}. \tag{27}$$

To visualize the dynamics on the $(\theta, \eta)$-plane for a given invariant value, we will iterate a grid of initial conditions. For each $(\theta, \eta)$, we first determine the radius, $r$, using the Newton method on $J(r\sin\eta\cos\theta, r\sin\eta\sin\theta, r\cos\eta)$, and then transform to Cartesian coordinates to obtain the initial point for (25). For subsequent iterates, we can simply project out the spherical

radius and plot $(\theta, \eta)$ along the orbit. To view the dynamics in the entire cube, we choose a grid in $J$ (from 1 to 0) and concatenate the figures to create the animations 60672_01.avi and 60672_02.avi. The animations reveal a system rich in complex, chaotic behavior.

Recall that when a map has an invariant, fixed points generically come in one-parameter families labeled by the invariant value [20]. Suppose that $\mathcal{O} = \{x_t, t = 0, \ldots, n-1\}$ is a periodic orbit of period $n$. Differentiating the equation $J(F^n(x)) = J(x)$ at the point $x_0$ gives

$$(DF^n(x_0))^T \cdot \nabla J(x_0) = \nabla J(x_0). \tag{28}$$

Thus when $\nabla J(x_0) \neq 0$ (as is true on all invariant surfaces except the origin and the fundamental cube), this vector is a left eigenvector of the Jacobian with unit multiplier. Since $F$ is volume-preserving, this implies that the multipliers of $\mathcal{O}$ are $(1, \lambda, \frac{1}{\lambda})$. When $\lambda \neq 1$, the implicit function theorem can be used to show there is a curve of fixed points of $F^n$ parameterized by $J$ through $x_0$. When $\lambda \neq \pm 1$, the periodic orbit is elliptic on the invariant surface if $\lambda$ is on the unit circle and hyperbolic when $\lambda$ is real. The orbit generically undergoes $q$-tupling bifurcations when $\lambda$ passes through the value $e^{2\pi i\omega}$ with $\omega = p/q$ rational. These bifurcations correspond to the creation of new periodic orbits of period $nq$; these new orbits are also found in one-parameter families parameterized by $J$.

To compute some of the low period orbits we use Broyden's method [16]. For the fixed points, we allowed the initial guess for Broyden's method to range over the entire invariant surface, so that we had a good chance of finding all of them. However, to limit the complexity of the figures, we decided only to search for periodic points born at the $q$-tupling bifurcations of the fixed points. An analytic expression for the Jacobian can be computed to determine the stability of the periodic points.

The analysis of fixed and periodic points gives us the ability to understand the fine structure of the system. It also illuminates any barriers to global transport on each invariant. For instance, the existence of large islands surrounding stable periodic points inhibits the transport of passive scalars. On the other hand, the existence of hyperbolic periodic points should aid transport due to the likelihood of homoclinic and heteroclinic tangles in their manifolds.

One measure of the degree of chaos in a system are its Lyapunov exponents. Since $F$ is volume-preserving, the sum of its three exponents must be zero, and because the orbits are restricted to two-dimensional surfaces, one of the exponents must be exactly equal to zero. This implies that the remaining two exponents are equal in magnitude and opposite in sign. We use the iterative $QR$ method to compute the exponents [21]. Along an orbit $\mathcal{O}$, define

$$Q^{(n+1)}\, R^{(n+1)} = DF(x_n)\, Q^{(n)}\, R^{(n)},$$

where $Q^{(0)} = R^{(0)} = id$. As usual $Q$ is orthogonal and $R$ is upper triangular. To compute the exponents, we require that $R_{ii} > 0$; it is not hard to show that one can modify the $QR$ method so that this is the case. Moreover, since $F$ is orientation-preserving and $\det(R) > 0$, then $Q \in SO(3)$. Thus we can represent $Q$ with three angles, $\theta_i$ (for example, Euler angles or rotations about three orthogonal axes). Since

$$R^{(n+1)}\, (R^{(n)})^{-1} = (Q^{(n+1)})^T\, DF(x_n)\, Q^{(n)}$$

is upper triangular, this requirement can be manipulated to provide a formula for updating the angles $\theta_i$ iteratively. After $n$ steps, the $i$th Lyapunov exponent is approximately

$$\lambda_i^{(n)} = \frac{\ln R_{ii}^{(n)}}{n} .$$

They can be computed iteratively using

$$\lambda_i^{(n)} = \frac{1}{n}\left((n-1)\lambda_i^{(n-1)} + \ln((Q^{(n)})^T\, DF(x_n)\, Q^{(n-1)})_{ii}\right).$$

We compute the exponents on a $(\theta, \eta)$ grid of initial conditions on each invariant surface. In order to resolve islands from the chaotic sea, a very fine grid is used and a large number of iterations are performed to get reasonable accuracy in the exponent. For all animations, Figures 11, 12, 15, and 16, 15000 iterations were performed on an $81 \times 51$ grid of initial conditions on each invariant surface.[2] We measure accuracy by averaging the standard deviation, $\langle\sigma\rangle$, of the final 1000 iterates over a given invariant via (29). As expected the accuracy depends strongly on the behavior in the phase plane. For the example given in section 7.1, we find $\langle\sigma\rangle = .0001$ when $J = .1$ and $\langle\sigma\rangle = .0115$ when $J = .8$. Between these values, an increasing trend is noted as the behavior evolves from regular to increasingly chaotic. For Figures 14 and 17, 15000 iterations were also performed on slightly smaller grids of size $81 \times 41$.

As an average measure of chaos on the invariant surface we compute the surface average of the positive Lyapunov exponent. The average of any function on a surface is approximated by

$$\langle f\rangle = \frac{1}{A}\sum_{i,j}^{n_\theta, n_\eta} f(x_{ij})\frac{|\nabla J(x_{ij})|\Delta\theta\Delta\eta}{|\det(DV(x_{ij})|}. \tag{29}$$

Here $|\nabla J|/|\det(DV)|$ is the surface area element with the Jacobian (27), $A$, the surface area, is determined so that $\langle 1\rangle = 1$, and $x_{ij}$ is the $ij$th point on the surface grid with spacing $\Delta\theta$ and $\Delta\eta$.

We expect the Lyapunov exponents will be very small near the origin, since the normal form analysis in section 6.1 indicates that orbits near the origin lie on invariant circles. Similarly the Lyapunov exponents near the boundary cube will tend toward those on the boundary faces. Recall that two of the boundary faces, $y = \pm\frac{\pi}{2}$, correspond to branches of the stable manifold of vertices. From (24), the Lyapunov exponents on these faces are $(-T_3, -T_1)$. However, on the four remaining faces, the dynamics are quite complex. We will see that the effect of the uniform faces is to decrease the Lyapunov exponents near the boundary.

**7.1. Example 1: $T_1 + T_3 = 12$.** We begin by exploring some of the dynamics of (25) for the case $T_1 = 7$, $T_3 = 5$. Recall that near the origin, the map is approximately a rotation about the axis $v_3$, where $v_3$ is the eigenvector of $DF(0)$ with eigenvalue one. In Figure 8 we show a projection of the dynamics onto the $(\theta, \eta)$-plane for $J$ near one; since $J = 1$ at the origin, the portrait shown in the figure corresponds to a small sphere near the origin. Most

[2] For the animations, Figures 12 and 16, 399 invariant values were used. The generation of the Lyapunov data took approximately two weeks to run on a Pentium 4 processor.

of the orbits lie on invariant circles, as suggested by the normal form analysis in section 6.1. The apparent change in topology of the circles in the figure is due only to nonalignment of the spherical projection with the rotation axis. Note that the reflection symmetry through the origin implies that the northern and southern hemispheres have conjugate dynamics.

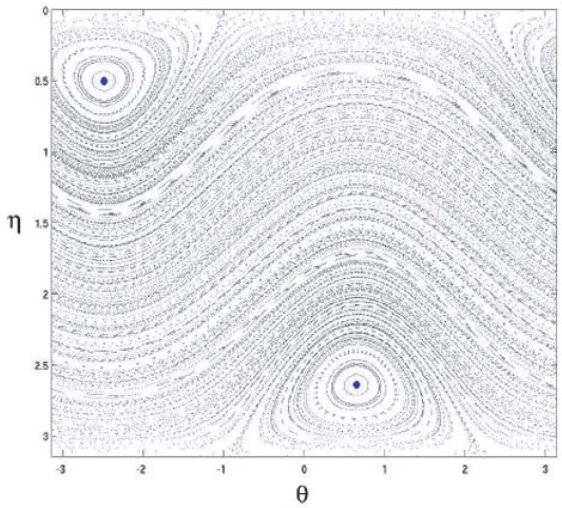


**Figure 8.** *Projection of the dynamics of* (25) *onto the* $(\theta, \eta)$*-plane for* $T_1 = 7, T_3 = 5$*, on the invariant surface* $J = 0.973962$.

There is a curve of fixed points tangent to the $v_3$-axis at the origin; this gives rise to a pair of fixed points on each invariant surface, and for these parameter values there are no other fixed points. We focus on the fixed point in the northern hemisphere—by symmetry the other fixed point has the same behavior. In Figure 9, we plot the multipliers $(1, \lambda, \lambda^{-1})$ of this fixed point as a function of $J$. Note that $J = 1$ at the top of the figure, corresponding to the origin in phase space, and $J$ decreases to 0 at the base of the figure, corresponding to the bounding cube. Several $q$-tupling bifurcations are labeled in the figure.

The phase space near several of these bifurcations is shown in Figure 10. In this figure the four panels on the left show the tripling bifurcation near $J \approx .61$ (corresponding to the squares in Figure 9). As is usual for area-preserving maps, there is a saddle-center bifurcation creating a pair of period-three orbits before the rotation number of the fixed point reaches $\frac{1}{3}$. In the interval $J \cong .628$ to $J \cong .623$, there is a bubble creating and destroying two new unstable period-three orbits in a pair of subcritical pitchfork bifurcations. As the rotation number approaches $\frac{1}{3}$, the saddle then collides with the fixed point at the tripling and later reappears on the opposite side. The bifurcation sequence is completed as the saddle-center pair experiences a subcritical saddle-center bifurcation thus annihilating the pair just after $J = .5508278$.

The four panels on the right show a sequence of period-two bifurcations near $J \approx .45$ (corresponding to the small bubble of instability in Figure 9). The first doubling is supercritical, resulting in the creation of a stable period-two orbit (the fixed point becomes unstable). Subsequently at $J \approx .448465$, the unstable fixed point undergoes a subcritical doubling event,

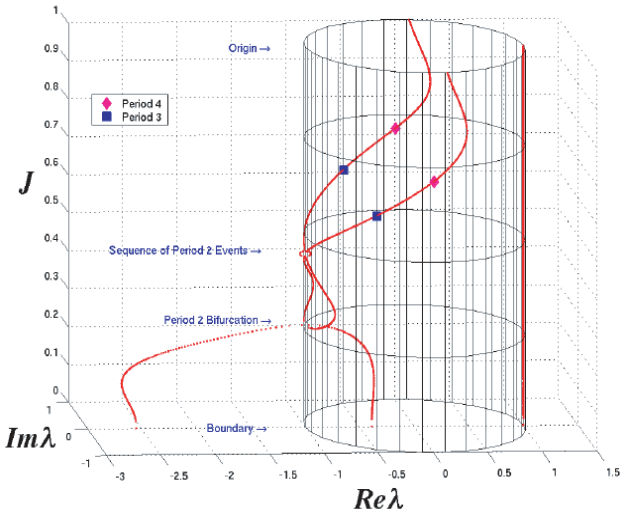


**Figure 9.** *Multipliers of the fixed point of* (25) *as a function of* $J$ *for* $T_1 = 7$ *and* $T_3 = 5$. *Doubling, tripling, and quadrupling bifurcations are noted.*

thus spawning an unstable period-two orbit. At $J \approx .448222$, the unstable period-two orbit created from the previous split undergoes a pitchfork bifurcation, thus creating a pair of unstable period-two orbits and a stable period-two orbit. When the sequence finishes, we have a stable fixed point, two stable period-two orbits, and two unstable period-two orbits. There is a final supercritical doubling of the fixed point near $J = 0.27$, and for all smaller values of $J$, the fixed points are unstable.

In the QuickTime file 60672_01.avi, we present an animation of the dynamics and maximal Lyapunov exponent for these parameter values. The movie consists of 399 frames starting at $J = .999$ and decreasing to $J = 0.002504$. For the dynamics panel, each initial condition on the grid of $14 \times 14$ points is iterated 1000 times.[3] Also shown in the movie are panels that display the position of the fixed point in space, and its multipliers in the complex plane. A snapshot of the animation is shown in Figure 11. The computations show a clear correspondence between the existence of island structures and small Lyapunov exponents. Outside of the islands, the Lyapunov exponent is nearly constant; however, there are several intervals of $J$ where invariant circles far from the fixed points reappear (they are mostly destroyed for $J < 0.75$), and this causes a local reduction in the chaos. In general, as $J$ decreases, the dynamics become more chaotic; though as $J$ nears zero the influence of the boundary dynamics appears in the animation by a concentration of chaotic motion near the edges of the cube and the reappearance of islands that correspond to stable fixed points on the boundary.

In Figure 12 we show the scaled surface average of the largest Lyapunov exponent, $\frac{\langle\lambda\rangle}{T}$ (where $T = T_1 + T_3$), as a function of $J$ using (29). Prominent bifurcations and characteristics

[3] Note the movie does not quite start and end at $J = 1$ and 0. $J = 1$ corresponds to the lone fixed point at the origin; thus we omitted this frame. For $J = 0$, the Lyapunov code exhibited extreme sensitivity which could not be resolved easily. In addition, close to bifurcation points, stability classification of fixed points is also numerically sensitive.

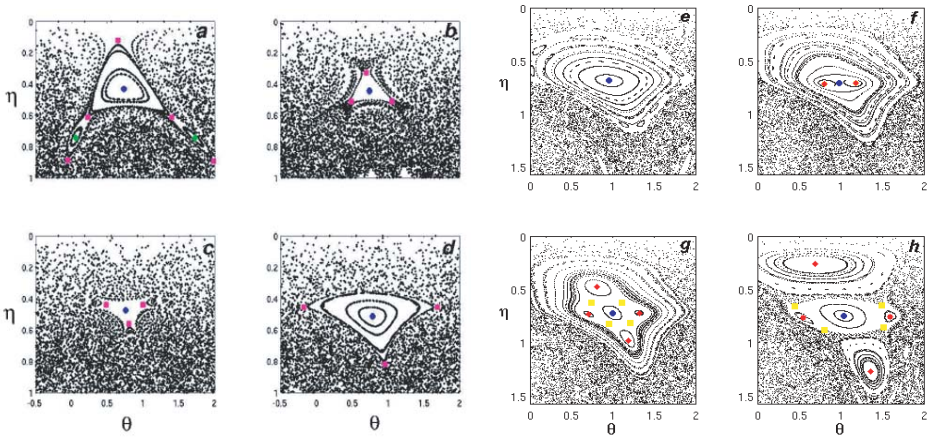


**Figure 10.** *Tripling and doubling bifurcations of a fixed point for* $T_1 = 7, T_3 = 5$. *The fixed point is shown as the blue circle, the green diamond and purple square correspond to stable and unstable period-three orbits, and the red diamond and yellow square are stable and unstable period-two orbits. The four panels at the left correspond to the following:* (a) $J = 0.625940$, *just after the first subcritical pitchfork bifurcation. (For resolution in our figures, the full phase plane is not shown. Hence one stable period-three point is omitted. Two additional unstable period-three points are shown (bottom left, bottom right) which are part of another unstable period-three orbit.)* (b) $J = 0.618429$, *just before tripling bifurcation.* (c) $J = 0.600902$. (d) $J = 0.578368$ *after the tripling. The right panels correspond to* (e) $J = 0.465699$ *and* (f) $J = 0.450677$, *just before and after the first supercritical doubling, and* (c) $J = 0.445669$ *and* (d) $J = 0.428143$, *after the second subcritical doubling and pitchfork bifurcations.*

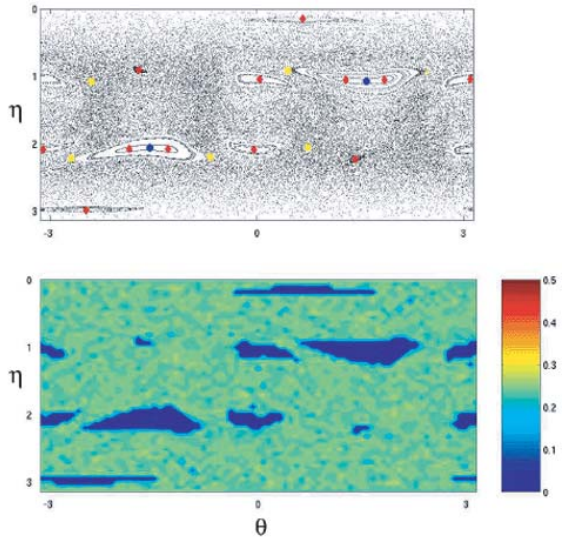


**Figure 11.** *Phase plane and the Lyapunov exponent for* $J = 0.262895$. *Points in the phase plane (upper panel) correspond to periodic orbits; colors are the same as in Figure* 10. *The bottom panel shows the largest Lyapunov exponent for a grid of initial conditions. Clicking on the above image displays the associated movie* (60672_01.avi).

of the phase portrait are indicated on the figure. The scaled average Lyapunov exponent remains nearly zero as $J$ decreases from 1, until near $J = 0.8$, when $\frac{\langle\lambda\rangle}{T}$ suddenly begins to increase. This suggests that the asymptotic validity of the normal form breaks down near this point and corresponds with the appearance of small zones of chaotic behavior. At the quadrupling and tripling bifurcations, $\frac{\langle\lambda\rangle}{T}$ reaches local maxima, and two local minima are associated with prominent period-two islands. The global maximum of $\frac{\langle\lambda\rangle}{T}$ occurs just inside the boundary, after which a steep decrease occurs. As we saw in section 6.2, this is to be expected because the Lyapunov exponents are negative on two of the six boundary faces.

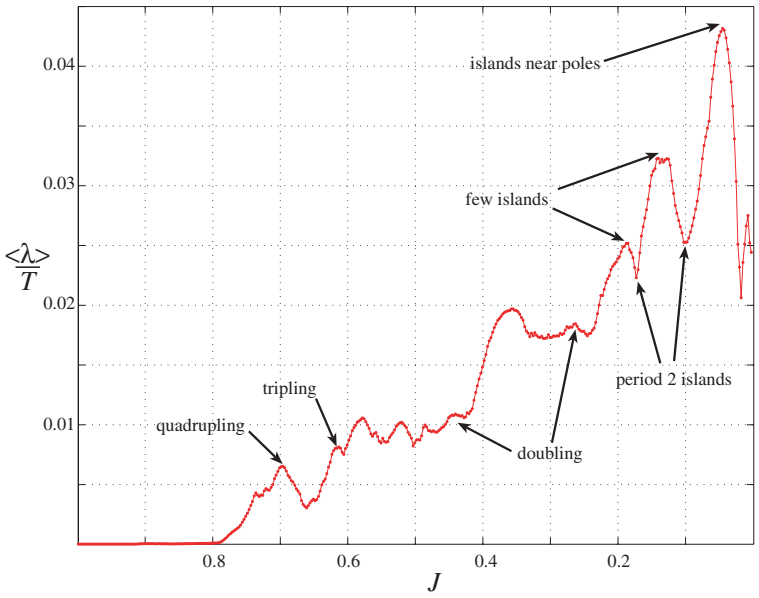


**Figure 12.** *Average scaled maximal Lyapunov exponent for* $T_1 = 7$, $T_3 = 5$.

Though three-dimensional mixing is forbidden by the existence of the invariant, mixing does occur on the invariant surfaces. To visualize this, we start a group of points in a small region (see Figure 13) and view them at successive times. Results of these computations reinforce the conclusion that limited transport occurs near the origin but that as $J$ decreases, mixing occurs on increasing scales and more rapidly. This mixing, however, is not complete, as islands can be seen in the panels even with the smallest values of $J$.

To explore the dependence of the Lyapunov exponents on the choice of parameters, we now fix $T_1 + T_3 = 12$ and vary the times in Figure 14. For each panel in the figure, $\frac{\langle\lambda\rangle}{T}$ is plotted as a function of $T_3$ for a fixed $J$. Note that each figure is symmetric about the point $T_1 = T_3$, as predicted by the symmetry analysis in section 5. This figure shows that there is no choice of $T_3$ such that $\frac{\langle\lambda\rangle}{T}$ is maximized on every invariant surface; however, there are large values of $\frac{\langle\lambda\rangle}{T}$ for most $J$ when $T_3 \approx 2$ or 10. This case might be expected to have the largest two-dimensional mixing on the surfaces of constant $J$.

The dynamics on the cubical boundary for this case are relatively uninteresting. The advection is so strong that the vast majority of iterates get pushed to the vertices or edges

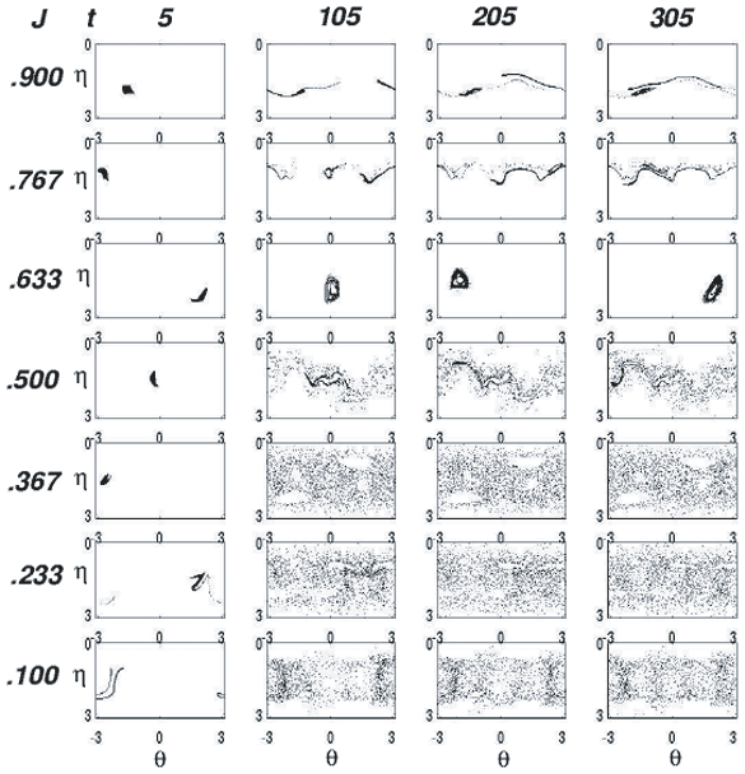


**Figure 13.** *Local mixing for* $T_1 = 7$, $T_3 = 5$. *Here a* $45 \times 45$ *grid of points is started in the region* $-\frac{\pi}{20} \le \theta \le \frac{\pi}{20}$ *and* $\frac{9\pi}{20} \le \eta \le \frac{11\pi}{20}$. *The rows correspond to different surfaces of constant* $J$ *and the columns to increasing numbers of iterates.*

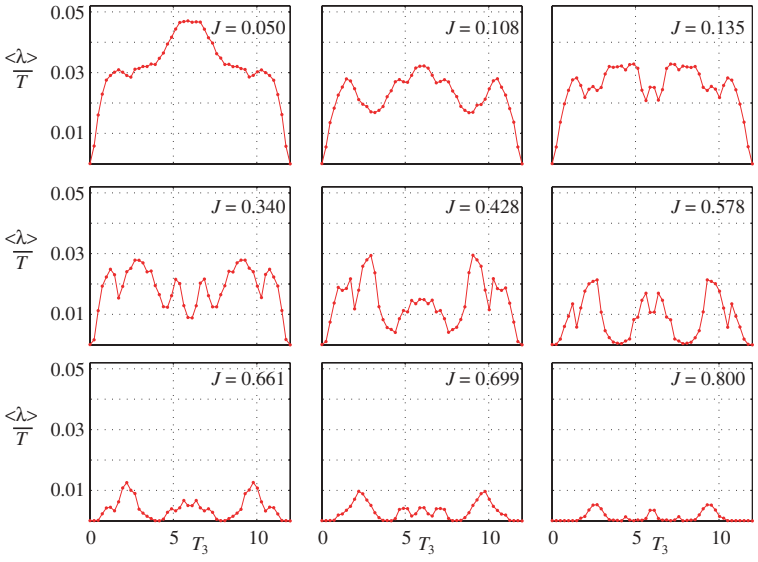


**Figure 14.** *Average Lyapunov exponent for varying* $T_3$ *with* $T_1 + T_3 = 12$.

almost immediately.

**7.2. Example 2: $T_1 + T_3 = 6$.** In this section we fix the total time to $T_1 + T_3 = 6$, half of the previous value. We will first consider the case $T_1 = 3.5$ and $T_3 = 2.5$ and see that the dynamics on the boundary has an influence that extends far into the interior of the cube.

We observe that for this case, as in section 7.1, there is a single curve of fixed points that emanates from the origin. The fixed points also have a bubble of instability that begins with a supercritical doubling near $J \approx 0.92$. Two new pairs of period-two orbits are born in saddle-center bifurcations near the poles when $J \approx 0.8$, and the new stable period-two orbits collide with the fixed points in a subcritical doubling at $J \approx 0.77$, completing the bubble. Unlike the previous case, the fixed points do not undergo another doubling bifurcation after they regain stability as $J$ continues to decrease; instead they remain stable (apart from a momentary instability at several tripling bifurcations) to $J = 0$. These fixed points continue to those on the boundary faces $x = \pm\frac{\pi}{2}$.

In Figure 15 we show two panels from the animation 60672_02.avi for this case. In the left panel, where $J = 0.282925$, there are large period-three islands surrounding the fixed point—these were born in a saddle-center bifurcation at $J \approx 0.306$. Islands from an earlier five-tupling bifurcation are also prominent (one of these islands encloses the pole and is thus hard to see in the projection). A band of regular behavior corresponding to invariant circles separates the surface into two invariant hemispheres; these have conjugate dynamics under the reflection symmetry $R$ in (15).

The right panel of Figure 15 shows the case $J = 0.030045$, close to the bounding cube. In this case there is an even larger band of meandering, invariant circles and a corresponding region of the small Lyapunov exponents. The boundary dynamics (recall Figure 6) strongly influences the dynamics on this surface. In the regions that correspond to the faces $y = \pm\frac{\pi}{2}$, the dominant motion sweeps the trajectories across the face and helps give rise to the invariant circles. Near the faces $x = \pm\frac{\pi}{2}$, the dynamics is predominantly chaotic, with the exception of small elliptic islands around the sole fixed point on each face.

In Figure 16 we show the average Lyapunov exponent as a function of $J$. As in Figure 12, $\frac{\langle\lambda\rangle}{T} \approx 0$ for an initial interval near the origin; however, now $\frac{\langle\lambda\rangle}{T}$ increases more or less monotonically, until $J \approx 0.22$, when it plunges rapidly to a local a minima at $J \approx 0.14$. This plunge occurs when the fixed points have multipliers that hover near the tripling point and seems to be associated with the creation of many modest size elliptic regions in the phase space. Note that the overall magnitude of $\frac{\langle\lambda\rangle}{T}$ is similar in this case to the previous one up until $J \approx .22$.

Finally, we show $\langle\lambda\rangle$ as a function of $T_3$ for $T_1 + T_3 = 6$ in Figure 17. Once again, there seems to be no consistent choice of $T_1$ and $T_3$ such that $\frac{\langle\lambda\rangle}{T}$ is maximized over every invariant. It is interesting to note, however, that near the origin, $\frac{\langle\lambda\rangle}{T}$ is maximized for equal times, in contrast with the results in Figure 14. However, as before, the largest Lyapunov exponents on most surfaces seem to occur when the time parameters substantially differ, in this case for $T_3 = 1.5$ or 4.5.

**8. Conclusions.** In 1984, Aref outlined a general, mathematically tractable stirring protocol for passive tracers chaotically advected by point vortices with specified location, strength, and lifetime. We have presented a simple, three-dimensional, incompressible flow analogous

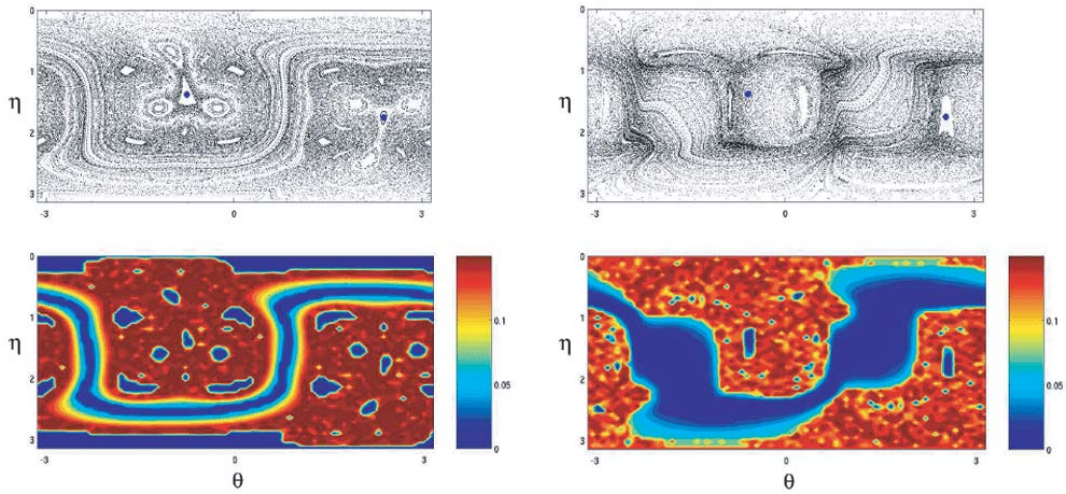


**Figure 15.** *Dynamics for $T_1 = 3.5$, $T_3 = 2.5$. The left panels correspond to $J = 0.282925$ and the right to $J = 0.030045$. Clicking on the above images displays the associated movie* (60672_02.avi).

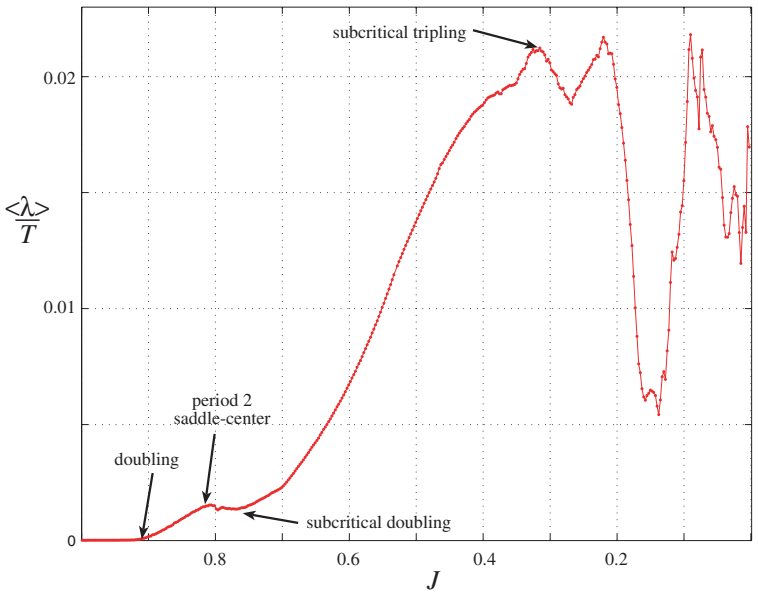


**Figure 16.** *Surface average of the maximal Lyapunov exponent as a function of $J$ for $T_1 = 3.5$, $T_3 = 2.5$.*

to Aref's two-dimensional blinking vortex model. In its most general form our model consists of a superposition of nonautonomous two-dimensional roll arrays. It simplifies considerably if the rolls act sequentially and are turned on and off instantaneously; for in this case, each two-dimensional flow lies on streamlines of the corresponding stream function. We have studied the case of orthogonal roll arrays with identical aspect ratio in detail, where the two-dimensional flow can be obtained analytically in terms of elliptic functions.

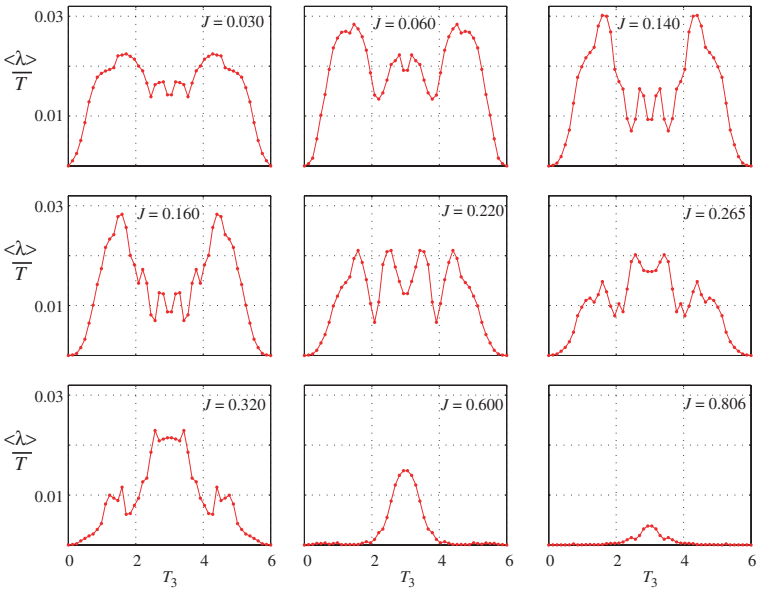


**Figure 17.** *Average Lyapunov exponent vs time, fixed invariants.*

For this case there is an invariant $J$, (14), so that the motion is confined to topological spheres. As shown in section 4, the invariant is a product of the orthogonality of the rolls and exists under any stirring protocol. Nevertheless, the dynamics on each two-dimensional surface can exhibit all of the complexity of area-preserving mappings. We have shown that the dynamics near the intersection of the centers of the rolls lies on families of invariant circles and can be described by an asymptotic normal form. The corresponding phase portraits show no chaos in this regime. The motion is constrained by the outermost boundary, which for our system is an invariant cube. Each face of the cube is invariant, and several of the faces have simpler dynamics corresponding to laminar shear and/or laminar shear followed by rotation. The onset of chaos occurs suddenly some distance from the origin, and, as measured by Lyapunov exponents, exhibits irregular growth as we continue to move away from the origin that is associated with bifurcations of fixed points and low period orbits.

In order to achieve true three-dimensional mixing in systems composed of roll arrays, the invariant must be broken. In [17], roll arrays of identical aspect ratio and axes given by $\hat{\mathbf{e}}_2$ and $\hat{\mathbf{e}}_3$ were positioned such that their respective intersections with the $\hat{\mathbf{e}}_1$-axis were 90° out of phase. Their investigations showed local and global three-dimensional mixing. Other possible constructions that may achieve three-dimensional mixing include (non)orthogonal roll arrays with identical/different aspect ratios. In the case of nearly orthogonal alternating roll arrays with identical aspect ratio, our preliminary investigations have shown that the invariant is in fact destroyed by this kind of perturbation. Initial studies indicate that the mixing near the intersection of roll axes is strongly influenced by the former invariant surfaces. This case also allows for transport between adjacent rolls. This case is unusual in a perturbation sense, since the unperturbed flow is chaotic itself. In the idealized limit where we consider infinite roll arrays, studies of transport throughout the domain can be understood under the framework of

anomalous diffusion theory [24, 27, 26, 25]. In a construction analogous to the Küppers–Lortz phenomenon, roll arrays rotating by 60° also display three-dimensional mixing. We will report on these topics in a future paper.

**Acknowledgments.** We would like to thank H. E. Lomelí and P. Boyland for helpful discussions.

## REFERENCES

[1] H. Aref, *Stirring by chaotic advection*, J. Fluid Mech., 143 (1984), pp. 1–21.
[2] H. Aref, *The development of chaotic advection*, Phys. Fluids, 14 (2002), pp. 1315–1325.
[3] D. Arrowsmith and C. Place, *An Introduction to Dynamical Systems*, Cambridge University Press, Cambridge, UK, 1990.
[4] A. Bazzani, *Normal form theory for volume-preserving maps*, Z. Angew. Math. Phys., 44 (1993), pp. 147–172.
[5] A. Bazzani and A. Di Sebastiano, *Perturbation theory for volume-preserving maps: Application to the magnetic field lines in plasma physics.*, in Analysis and Modelling of Discrete Dynamical Systems, Adv. Discrete Math. Appl. 1, Gordon and Breach, Amsterdam, 1998, pp. 283–300.
[6] G. Birkhoff, *Surface transformations and their dynamical applications*, Acta Math., 43 (1920), pp. 1–119.
[7] P. Boyland, *personal communication*, 2003.
[8] M. Brown and K. Smith, *Ocean stirring and chaotic low-order dynamics*, Phys. Fluids, 3 (1991), pp. 1186–1192.
[9] F. Busse and K. E. Heikes, *Convection in a rotating layer—simple case of turbulence*, Science, 208 (1980), pp. 173–175.
[10] P. F. Byrd and M. D. Friedman, *Handbook of Elliptic Integrals for Engineers and Physicists*, Springer-Verlag, New York, 1954.
[11] J. Cartwright, M. Feingold, and O. Piro, *Chaotic advection in three dimensional unsteady incompressible laminar flow*, J. Fluid Mech., 316 (1996), pp. 259–284.
[12] J. H. E. Cartwright, M. O. Feingold, and O. Piro, *Passive scalars and three-dimensional Liouvillian maps*, Phys. D, 76 (1994), pp. 22–33.
[13] T. Dombre, U. Frisch, J. Greene, M. Hénon, A. Mehr, and A. Soward, *Chaotic streamlines in the ABC flows*, J. Fluid Mech., 167 (1986), pp. 353–391.
[14] C. Elphick, E. Tirapegui, M. Brachet, P. Coullet, and G. Iooss, *A simple global characterization for normal forms of singular vector fields*, Phys. D, 29 (1987), pp. 95–127.
[15] M. Feingold, L. Kadanoff, and O. Piro, *Passive scalars, three-dimensional volume-preserving maps, and chaos*, J. Statist. Phys., 50 (1988), pp. 529–565.
[16] B. P. Flannery, W. H. Press, S. A. Teukolsky, and W. T. Vetterling, *Numerical Recipes in C, The Art of Scientific Computing*, 2nd ed., Cambridge University Press, Cambridge, UK, 1992.
[17] M. Fogleman, M. Fawcett, and T. Solomon, *Lagrangian chaos and correlated Lévy flights in a non-Beltrami flow: Transient versus long-term transport*, Phys. Rev. E (3), 63 (2001), pp. 1–4.
[18] G. Fountain, F. Khakhar, and J. Ottino, *Visualization of three-dimensional chaos*, Science, 281 (1998), pp. 683–686.
[19] G. O. Fountain, D. V. Khakhar, I. Mezic, and J. Ottino, *Chaotic mixing in a bounded three-dimensional flow*, J. Fluid Mech., 417 (2000), pp. 265–301.
[20] A. Gomez and J. Meiss, *Volume-preserving maps with an invariant*, Chaos, 12 (2002), pp. 289–299.
[21] S. Habib, T. Janaki, G. Rangarajan, and R. D. Ryne, *Computation of the Lyapunov spectrum for continuous-time dynamical systems and discrete maps*, Phys. Rev. E (3), 60 (1999), pp. 6614–6626.
[22] Y. Hu, W. Pesch, G. Ahlers, and R. Ecke, *Convection under rotation for Prandtl numbers near* 1: *Küppers-Lortz instability*, Phys. Rev. E (3), 58 (1998), pp. 5821–5833.
[23] C. Jones and S. Winkler, *Invariant manifolds and Lagrangian dynamics in the ocean and atmosphere*, in Handbook of Dynamical Systems, Vol. 2, North–Holland, Amsterdam, 2002, pp. 55–92.

[24] J. Klafter, A. Blumen, and M. Shlesinger, *Stochastic pathway to anomalous diffusion*, Phys. Rev. A (3), 35 (1987), pp. 3081–3085.
[25] J. Klafter, M. Shlesinger, and G. Zumofen, *Beyond Brownian motion*, Physics Today, 49 (1996), pp. 33–39.
[26] J. Klafter, G. Zumofen, and M. Shlesinger, *Anomalous diffusion and Lévy statistics in intermittent chaotic systems*, in Chaos: The Interplay between Stochastic and Deterministic Behavior, Lecture Notes in Phys. 457, Springer-Verlag, Berlin, 1995, pp. 183–210.
[27] J. Klafter, G. Zumofen, M. Shlesinger, and A. Blumen, *Scale invariance in anomalous diffusion*, Philosophical Magazine B, 65 (1992), pp. 755–765.
[28] G. Küppers and D. Lortz, *Transition from laminar convection to thermal turbulence in a rotating fluid layer*, J. Fluid Mech., 35 (1969), pp. 609–620.
[29] H. Lomelí and J. Meiss, *Quadratic volume-preserving maps*, Nonlinearity, 11 (1998), pp. 557–574.
[30] H. Lomelí and J. Meiss, *Heteroclinic primary intersections and codimension one Melnikov method for volume-preserving maps*, Chaos, 10 (2000), pp. 109–121.
[31] H. E. Lomelí and J. Meiss, *Heteroclinic orbits between invariant circles in volume-preserving mappings*, Nonlinearity, 16 (2003), pp. 1573–1595.
[32] C. Lopez, E. Hernandez-Garcia, O. Piro, A. Vulpiani, and E. Zambianchi, *Population dynamics advected by chaotic flows: A discrete-time map approach*, Chaos, 11 (2001), pp. 397–403.
[33] G. Metcalfe, T. Shinbrot, J. McCarthy, and J. M. Ottino, *Avalanche mixing of granular solids*, Nature, 374 (1995), pp. 39–41.
[34] E. Moses and V. Steinberg, *Stationary convection in a binary mixture*, Phys. Rev. A (3), 43 (1991), pp. 707–722.
[35] Z. Neufield, P. Haynes, and T. Tel, *Chaotic mixing induced transitions in reaction-diffusion systems*, Chaos, 12 (2002), pp. 426–438.
[36] J. Ottino, *The Kinematics of Mixing: Stretching, Chaos, and Transport*, Cambridge University Press, Cambridge, UK, 1989.
[37] O. Piro and M. Feingold, *Diffusion in three-dimensional Liouvillian maps*, Phys. Rev. Lett., 61 (1988), pp. 1799–1802.
[38] L. Rom-Kedar, V. Kadanoff, E. Ching, and C. Amick, *The break-up of a heteroclinic connection in a volume preserving mapping*, Phys. D, 62 (1993), pp. 51–65.
[39] I. Scheuring, G. Karolyi, Z. Toroczkai, T. Tel, and A. Pentek, *Competing populations in flows with chaotic mixing*, Theoretical Populational Biology, 63 (2003), pp. 77–90.
[40] T. Shinbrot, M. Alvarez, J. Zalc, and F. Muzzio, *Attraction of minute particles to invariant regions of volume preserving flows by transients*, Phys. Rev. Lett., 86 (2001), pp. 1207–1210.
[41] A. Stroock, S. Dertinger, A. Ajdari, I. Mezic, H. Stone, and G. Whitesides, *Chaotic mixer for microchannels*, Science, 295 (2002), pp. 647–651.
[42] R. Toral, M. San Miguel, and R. Gallego, *Period stabilization in the Busse-Heikes model of the Küppers-Lortz instability*, Phys. A, 280 (2000), pp. 315–336.
[43] Y. Tu and M. Cross, *Chaotic domain structure in rotating convection*, Phys. Rev. Lett., 69 (1992), pp. 2515–2518.